ACS APPLIED MATERIALS & INTERFACES
Research Article
www.acsami.org

Fabrication of Core–Shell α-Fe_2O_3@ $Li_4Ti_5O_{12}$ Composite and Its Application in the Lithium Ion Batteries

Ming Chen, Wei Li, Xiao Shen, and Guowang Diao*

College of Chemistry and Chemical Engineering, Yangzhou University, Yangzhou 225002, P. R. China

Key Laboratory of Environmental Materials & Environmental Engineering of Jiangsu Province, Yangzhou 225002, Jiangsu, P. R. China

Supporting Information

ABSTRACT: In this work, a novel carbon-free core–shell α-iron oxide (α-Fe_2O_3)@ spinel lithium titanate ($Li_4Ti_5O_{12}$, LTO) composite has been synthesized via a facile hydrothermal process. Element mapping confirmed the core–shell structure of α-Fe_2O_3@LTO. The effects of various experimental parameters, including thickness of TiO_2 coating, reaction temperature, and time on the morphologies of the resulted products, were systematically investigated. The electrochemical measurements demonstrate that uniform α-Fe_2O_3 ellipsoids are coated with LTO to avoid forming a solid electrolyte interface (SEI) layer, to reduce initial capacity loss, and to improve the reversibility of α-Fe_2O_3 for Li ion storage. Compared with naked α-Fe_2O_3 ellipsoids, the α-Fe_2O_3@LTO composites exhibit lower initial capacity loss, higher reversible capacity, and better cycling performance for lithium storage. The electrochemical performance of α-Fe_2O_3@LTO composite heavily depends on the thickness and density of LTO coating shells. The carbon-free coating of LTO is highly effective in improving the electrochemical performance of α-Fe_2O_3, promising advanced batteries with high surface stability and excellent security.

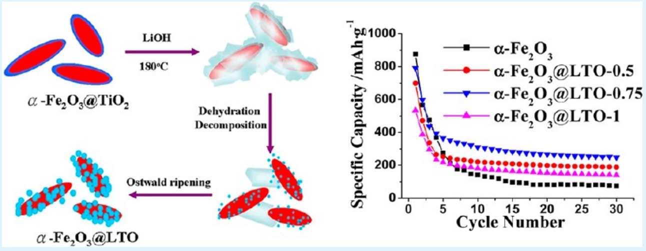

KEYWORDS: *α-Fe_2O_3, lithium titanate, core–shell structure, carbon-free anode materials, Li ion batteries*

1. INTRODUCTION

Lithium-ion batteries (LIBs), a rapidly developing technology in energy storage, are most important as power sources for a wide range of portable electronic devices.[1−3] However, graphite, the anode material currently used in commercial LIBs, has a relatively low Li storage capacity of 350 mA h g^{-1}.[1] In addition, carbonaceous anode materials have the risk of safety problems when operating under high current densities such as power sources. Hence, to meet the ever-increasing performance demands and to overcome safety issues, the search for alternative anode materials has become a consequential task in fabricating the next-generation of LIBs. Many transition metal oxides have been investigated as anode materials for lithium ion batteries.[4−14] α-Iron oxide (α-Fe_2O_3), an important member of the metal oxide family, is believed to be a promising candidate to replace graphite, because it has a much higher theoretical capacity of 1005 mA h g^{-1} than that of commercial graphite anode materials and is relatively easy to synthesize by environmentally friendly methods from low-cost resources. Thus, the investigation of α-Fe_2O_3 as a lithium ion storage material represents a potentially worthwhile pursuit in the search for new anode materials with high capacity for lithium ion batteries.[15−24]

Nowadays, the development of these high-capacity anode materials, especially transition metal oxides, has been met with two significant challenges: high initial capacity loss and capacity fading in prolonged cycling. Some irreversible secondary reactions, such as the formation of a solid electrolyte interface (SEI), result in initial capacity loss.[25−27,8] The large volume excursion brings about capacity fading in lithium insertion and extraction reactions, which leads to anode cracking and loss of electrical connectivity.[25] To overcome the above difficulties, novel nanostructure design and preparation of composites have been regarded as the most efficient methods.[17,18,23,28−30] Nanostructure may reduce the Li ion diffusion length and enhance the tolerance to strains caused by the Li ion insertion/extraction reactions. For example, hollow spheres of α-Fe_2O_3 exhibit greatly enhanced Li storage properties, with a reversible capacity as high as 710 mA h g^{-1}, even after 100 charge–discharge cycles.[23] The RG-O/Fe_2O_3 composites display discharge and charge capacities of ~1355 and 982 mA h g^{-1}, respectively (based on the total mass of the composite), with good cycling performance and rate capability.[28] Zhou et al. synthesized an epitaxial growth of branched α-Fe_2O_3/SnO_2 nanoheterostructure, which shows low initial irreversible loss and high reversible capacity.[31]

Recently, among the candidates of anode materials, spinel $Li_4Ti_5O_{12}$ (LTO) as a star material has attracted considerable

Received: January 14, 2014
Accepted: March 5, 2014
Published: March 5, 2014

dx.doi.org/10.1021/am500294m | ACS Appl. Mater. Interfaces 2014, 6, 4514−4523

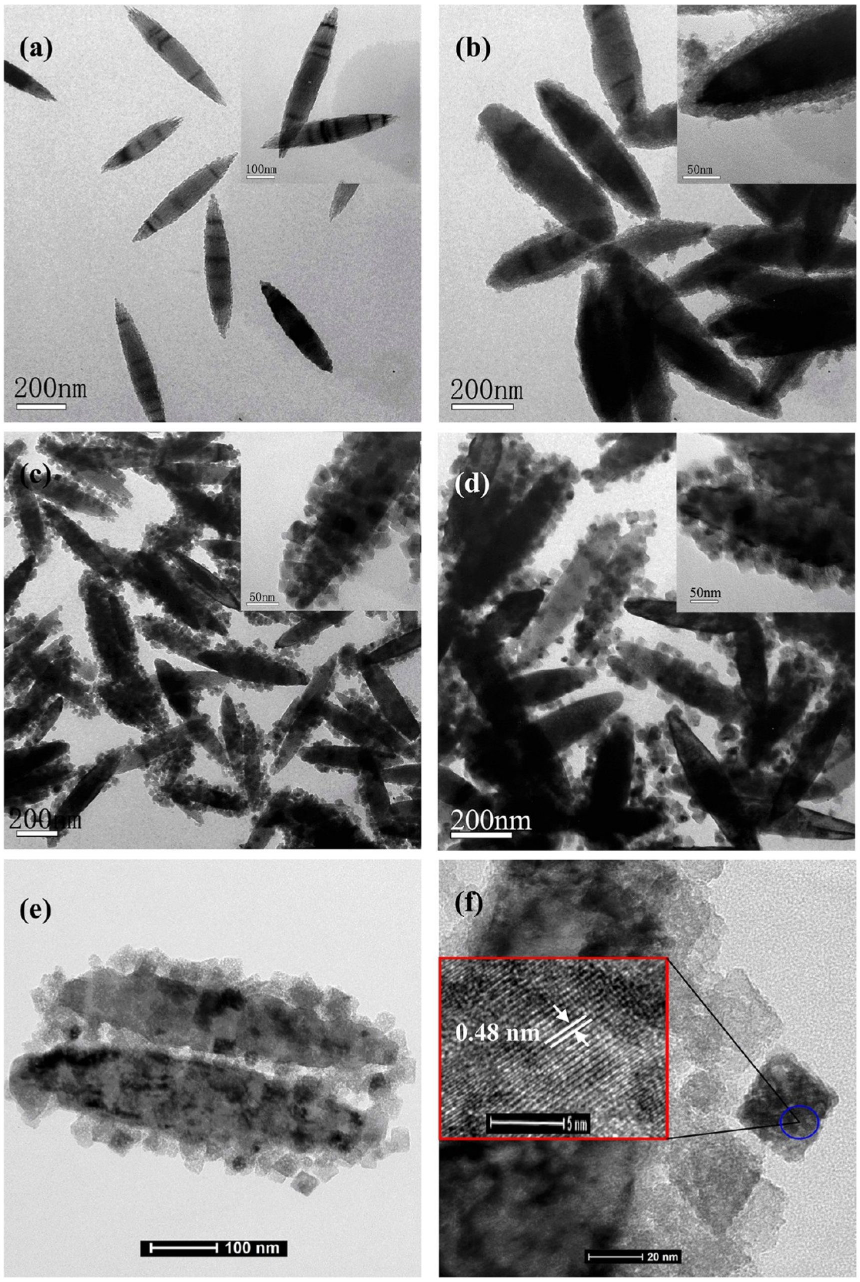

Figure 1. TEM images of (a) α-Fe_2O_3, (b) α-Fe_2O_3@TiO_2-0.75, (c) before calcination of α-Fe_2O_3@LTO-0.75, (d) after calcination of α-Fe_2O_3@LTO-0.75, and (e),(f) HRTEM image after calcination of α-Fe_2O_3@LTO-0.75 with different magnifications.

attention because of its intrinsic characteristics.[32−36] Firstly, it has a higher Li-insertion voltage (ca. 1.5 V vs Li^+/Li) than that of commercial graphite anode (below 0.2 V vs Li^+/Li). So, $Li_4Ti_5O_{12}$ can avoid reduction of the electrolyte on the surface of the electrode and formation of a SEI layer (usually occurring below 1.0 V Li^+/Li).[37,38] Secondly, spinel $Li_4Ti_5O_{12}$ is a zero-strain insertion material, which has excellent reversibility in lithium insertion/extraction reactions.[39,40] These two features make it a promising anode material for lithium ion batteries used in the fields of hybrid electric vehicles and large-scale energy storage, in which long cycle life, high safety, and high power density are highly desired.[41−43]

Herein, we reported a new method to synthesize α-Fe_2O_3@LTO composites via a three-step process. The advantages of using LTO to improve α-Fe_2O_3 in LIBs applications are investigated in this paper. The results showed that the LTO coating shielded most of the direct contact between α-Fe_2O_3 and the electrolyte, and hence the SEI formation was reduced to mostly that of LTO. Additionally, the α-Fe_2O_3@LTO composites also showed notable improvements in material cyclability and rate performance.

2. EXPERIMENTAL SECTION

2.1. Materials. $FeCl_3 \cdot 6H_2O$, tetrabutyl titanate (TBOT), concentrated ammonia solution (28 wt %), $LiOH \cdot H_2O$, and polyvinylidene difluoride (PVDF) were of analytical grade and purchased from Shanghai Chemical Corp. French Arkema The electrolyte solution with 1 M $LiPF_6$/ethylene carbonate (EC)/diethyl carbonate (DMC)/ethyl methyl carbonate (EMC) (1:1:1 by volume) was purchased from Guangzhou Tinci Materials Technology Co., Ltd. Other chemicals and solvents are reagent grade and commercially available. Deionized water was used for all experiments.

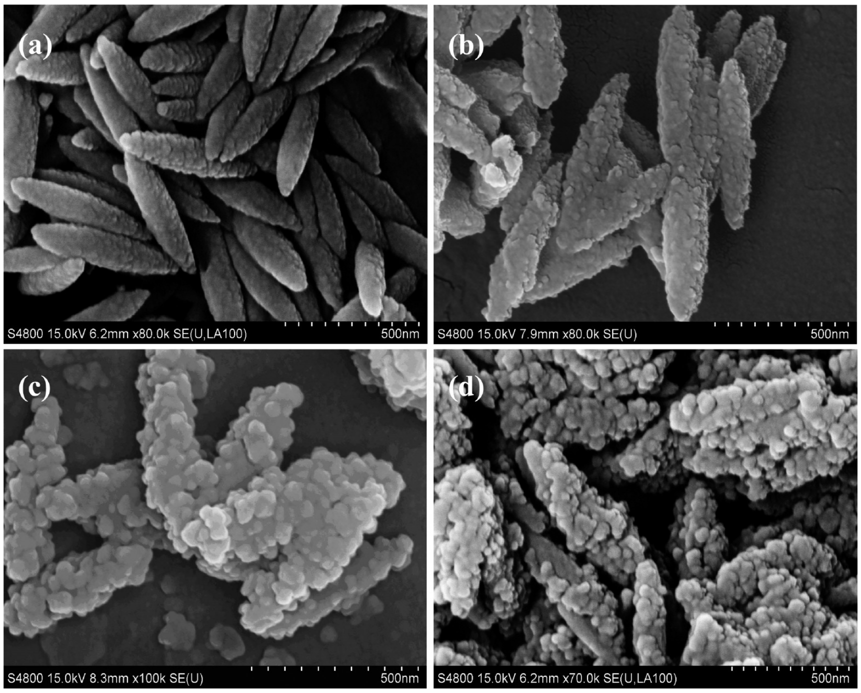

Figure 2. SEM images of (a) α-Fe_2O_3, (b) α-Fe_2O_3@TiO_2-0.75, (c) before calcination of α-Fe_2O_3@LTO-0.75, and (d) after calcination of α-Fe_2O_3@LTO-0.75.

2.2. Characterization. TEM (transmission electron microscopy) observation was conducted on a Philips TECNAI-12 instrument. SEM was applied to investigate the morphology, which was carried out with Hitachi S-4800 (Japan). High-resolution TEM (HRTEM) and energy-dispersive X-ray (EDX) were performed on a FEI Tecnai G2 F30 S-TWIN (U.S.A.) operating at 200 kV. Diffraction (XRD) data were obtained with a graphite monochromator and Cu Kα radiation (λ = 0.1541 nm) on a D8 advance superspeed powder diffractometer (Bruker). Cyclic voltammograms were carried out with a CHI660c electrochemical workstation (Chenghua, China).

2.3. Preparation of α-Fe_2O_3@LTO Composites. *Synthesis of α-Fe_2O_3 Ellipsoids.* The α-Fe_2O_3 ellipsoids were prepared by aging a solution of $FeCl_3$ (0.54 g), KH_2PO_4 (0.0061 g), and 100 mL of H_2O at 105 °C for 48 h.[44] The obtained products were separated and collected by centrifugation, followed by washing with deionized water and ethanol for 3 times, respectively.

Synthesis of α-Fe_2O_3@TiO_2 Core−Shell Nanostructures. The uniform TiO_2 shell core−shell structures were prepared via the versatile kinetics-controlled coating method.[44] The α-Fe_2O_3 ellipsoids (0.075 g) were dispersed in absolute ethanol (100 mL) and mixed with concentrated ammonia solution (0.30 mL, 28 wt %) under ultrasound for 15 min. Afterward, 0.75 mL of TBOT was added dropwise in 5 min, and the reaction was allowed to proceed for 24 h at 45 °C under continuous mechanical stirring. The resultant products were separated and collected, followed by washing with deionized water and ethanol for 3 times, respectively. Then, the obtained powders were dried at 100 °C overnight.

Synthesis of α-Fe_2O_3@LTO Composite. The α-Fe_2O_3@TiO_2 composites and 0.125 g (1.5 mmol) $LiOH\cdot H_2O$ were ultrasonically dispersed in 15 mL of deionized water. Then, the mixture was transferred to a 25 mL Teflon-lined reactor. The reactor was heated to 180°C and kept at this temperature for 24 h to form a lithium titanate coating on the α-Fe_2O_3 ellipsoids. The solid phase was recovered by centrifugation, followed by washing with ethanol and deionized water and vacuum drying at 50°C for 12 h. The final product was obtained after calcination at 500°C for 2 h.

2.4. Electrochemical Tests. The anode electrode was prepared by mixing the calcined α-Fe_2O_3@LTO samples (80%) with 10 % acetylene black as a conductive material and 10 % polyvinylidene difluoride (PVDF) binder dissolved in *N*-methyl-2-pyrrolidinone (NMP). Then, the slurries of the mixture were cast onto an aluminium foil current collector. After coating, the electrodes were dried at 80 °C for 4 h to remove the solvent before pressing. The electrodes were punched in the form of disks and then vacuum dried at 120 °C for 12 h. The cell (CR 2032 coin-type cell) assembly was operated in a glove box (Vacuum Atmospheres Co., Ltd) filled with high purity argon. The cells were assembled with the as-prepared positive electrode, lithium metal, and separators made of a Celgard 2400 film. The electrochemical tests of the samples were evaluated at constant discharge and charge current densities in the 0.5 V to 2.5 V voltage window by using an automatic battery testing system (Neware, CT-3008W).

3. RESULTS AND DISCUSSION

3.1. Characterization of α-Fe_2O_3@LTO Composites. The morphologies of α-Fe_2O_3 ellipsoids, uniform core−shell α-Fe_2O_3@TiO_2 microellipsoids, and α-Fe_2O_3@LTO composites before and after calcination were characterized using TEM. Uniform α-Fe_2O_3 ellipsoids are first synthesized with a diameter of ∼100 nm and length of ∼500 nm as the cores (Figure 1a). Then, via a sol−gel reaction of TBOT (0.75 mL) in ethanol/ammonia mixtures, core−shell α-Fe_2O_3@TiO_2 microellipsoids (labeled as α-Fe_2O_3@TiO_2-0.75) are obtained with a diameter of ∼150 nm and length of ∼580 nm (Figure 1b). The thickness of the amorphous TiO_2 shell is ∼25 nm (inset of Figure 1b). Lastly, the preparation of α-Fe_2O_3@TiO_2-0.75 reacts with LiOH to form α-Fe_2O_3@LTO composites (labeled as α-Fe_2O_3@LTO-0.75). The morphology of the α-Fe_2O_3@LTO-0.75 composite is shown in Figure 1c. α-Fe_2O_3@LTO-0.75 composite shows a new style core−shell structure. Actually, LTO nanoparticles with irregular shape coat on the surface of α-Fe_2O_3. The average diameter of nanoparticles of LTO is about 25 nm. After calcination of α-Fe_2O_3@LTO-0.75, the morphology of the α-Fe_2O_3@LTO-0.75 composite has no essential change (Figure 1d). For better understanding the dimensionality of the α-Fe_2O_3@LTO-0.75 composite morphology, high-resolution transmission electron microscopy

(HRTEM) is recorded. It is clearly shown that a large number of LTO nanoparticles coat on the surface of α-Fe_2O_3 to form core−shell α-Fe_2O_3@LTO. Some LTO nanoparticles show the distinct diamond shape. The lattice resolved HRTEM image of LTO nanocrystal is shown in Figure 1f. Inter planar spacing of 4.8 Å corresponds well with the spinel structure $Li_4Ti_5O_{12}$ (111) plane.

The morphologies of α-Fe_2O_3 ellipsoids, uniform core−shell α-Fe_2O_3@TiO_2 microellipsoids, and α-Fe_2O_3@LTO composites before and after calcination were also confirmed by scanning electron microscopy (SEM). In Figure 2a, uniform α-Fe_2O_3 ellipsoids have a smooth surface. The core−shell α-Fe_2O_3@TiO_2 microellipsoids display rough surface, which confirms that amorphous TiO_2 shells coat on α-Fe_2O_3 cores (Figure 2b). Compared with α-Fe_2O_3@TiO_2, LTO nanoparticles embed the surface of α-Fe_2O_3, and the surface roughness increases (Figure 2c). After calcination of α-Fe_2O_3@LTO-0.75, the morphology of the α-Fe_2O_3@LTO-0.75 composite is unchanged (Figure 2d), which corresponds to the result of TEM images.

The chemical composition of these samples is analyzed by X-ray diffraction (XRD). In Figure 3a, all the identified diffraction peaks are unambiguously assigned to the phase pure rhombohedral Fe_2O_3 (JCPDS card no. 33-0664). When the amorphous TiO_2 coats on α-Fe_2O_3 (Figure 3b), the XRD pattern still shows the diffraction peaks of α-Fe_2O_3. For the α-Fe_2O_3@LTO-0.75 composite (Figure 3c), three additional peaks appear at 18.4°, 43.4°, and 57.2°, which correspond well with the (111), (400), and (333) diffractions of spinel lithium titanate (JCPDS card no. 49-0207). After calcination, the intensity of the LTO peaks increases.

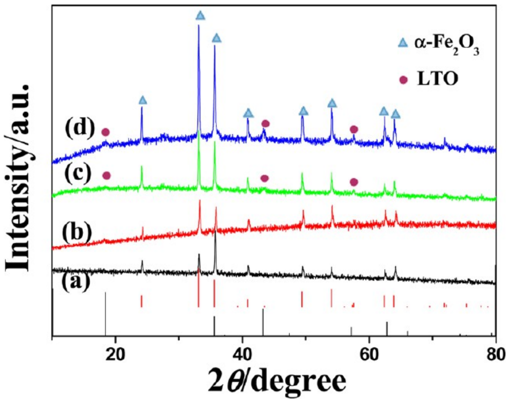

Figure 3. XRD patterns of (a) α-Fe_2O_3, (b) α-Fe_2O_3@TiO_2-0.75, (c) before calcination of α-Fe_2O_3@LTO-0.75, and (d) after calcination of α-Fe_2O_3@LTO-0.75. The vertical lines are the standard XRD patterns of hematite α-Fe_2O_3 (JCPDS card no. 33-0664) (red line) and spinel lithium titanate (JCPDS card no. 49-0207) (black line).

The core−shell structure and the composition of the composite are ascertained by the element maps from energy-dispersive X-ray (EDX) spectroscopy. The distributions of Fe, O, and Ti are shown in Figure 4. The core area clearly displays the existence of Fe. The presence of titanium is only confined to the shell area. The oxygen element distributes in both the core area and the shell area. Therefore, the element maps from EDX confirm the core−shell structure of α-Fe_2O_3@LTO composite.

3.2. Formation Mechanism of α-Fe_2O_3@LTO Composite.

3.2.1. Effect of the Thickness of the TiO_2 Coating. First, the thickness of shell is adjusted by changing the thickness of the amorphous TiO_2 coating, which could be varied by controlling the amount of TBOT used (0.5 mL and 1.0 mL of TBOT, labeled as α-Fe_2O_3@TiO_2-0.5 and α-Fe_2O_3@TiO_2-1, respectively). In the TEM images of α-Fe_2O_3@TiO_2-0.5 and α-Fe_2O_3@TiO_2-1 in Figure 5a,c, the uniform coating are formed on the surface of α-Fe_2O_3 and the shells' thicknesses are 10 and 80 nm, respectively. In addition, in Figure 5c, core−shell α-Fe_2O_3@TiO_2-1 microellipsoids show a certain degree of conglutination and aggregation. Two α-Fe_2O_3@TiO_2 composites were reacted with LiOH and calcined to form α-Fe_2O_3@LTO composites shown in Figure 5b,d (labeled as α-Fe_2O_3@LTO-0.5 and α-Fe_2O_3@LTO-1). It is clear that a few of LTO nanocrystals coat the surface of α-Fe_2O_3 in Figure 5b. With small thickness of the amorphous TiO_2 coating, the composite is unable to form the complete core−shell structure. On the contrary, large amounts of LTO nanocrystals embed the surface of α-Fe_2O_3 to form the core−shell structure at the larger thickness of the TiO_2 coating. The thichness of the LTO shell is about 80 nm, which equals to the thickness of the TiO_2 coating. Compared with the α-Fe_2O_3@LTO-0.75 (Figure 1d), the thickness of the LTO increases markedly, and the LTO shell becomes compact. Therefore, the thickness of shells in core−shell α-Fe_2O_3@LTO can be effectively adjusted by controlling the thickness of the TiO_2 coating. SEM images of these samples also confirm this view. XRD data further demonstrate that the chemical compositions of these samples are α-Fe_2O_3@LTO composites (Figure 6). Obviously, with the increase of the thickness of the coated layer, the intensity of these LTO peaks increases evidently. The Ti/Fe ratios in α-Fe_2O_3@LTO-0.5, α-Fe_2O_3@ LTO-0.75, and α-Fe_2O_3@ LTO-1 were determined to be 1:45, 1:21, and 1:12 by EDX, which are consistent with the increasingly thicker shells. The corresponding weight fractions of LTO in three composites are 2.5%, 5.2%, and 8.7% respectively.

3.2.2. Effect of the Reaction Temperature. The effect of reaction temperature was studied. In typical reaction, α-Fe_2O_3@TiO_2 composite reacts with LiOH at 180 °C. Then, the reaction proceeds at 150 °C and 210 °C, respectively. The morphologies of products obtained are shown in Figure 7a, b. It is obvious that a small number of LTO nanocrystals adsorb on the surface of α-Fe_2O_3 at 150 °C (in Figure 7a). Furthermore, some nanosheets (red arrows) appear in the sample, which are intermediate products confirmed by the effect of reaction time. At higher temperature (210 °C), LTO nanocrystals scatter around the α-Fe_2O_3 and do not coat on the surface of α-Fe_2O_3 to form LTO shell (in Figure 7c). After calcination, the morphologies of the α-Fe_2O_3@LTO-0.75 composites obtained at 150 °C and 210 °C are shown in Figure 7b and Figure 7d, respectively. The amount of LTO nanocrystals coating on the surface of α-Fe_2O_3 increases comparing to before calcination, indicating the decomposition of intermediate products at higher temperature (Figure 7b). After the calcination of the sample obtained at 210 °C, a few of LTO nanocrystals coat the surface of α-Fe_2O_3 (Figure 7d). Compared with the product prepared at 180 °C, the products obtained at 150 °C and 210 °C do not form the whole core−shell structure, which indicates that suitable temperature is beneficial to enhance affinity between α-Fe_2O_3 and LTO and promote the formation of core−shell structure. The crystal structure of the samples obtained at different reaction temperature was examined using XRD and the results are shown in Figure S1 (Supporting Information). XRD patterns show that the position and relative

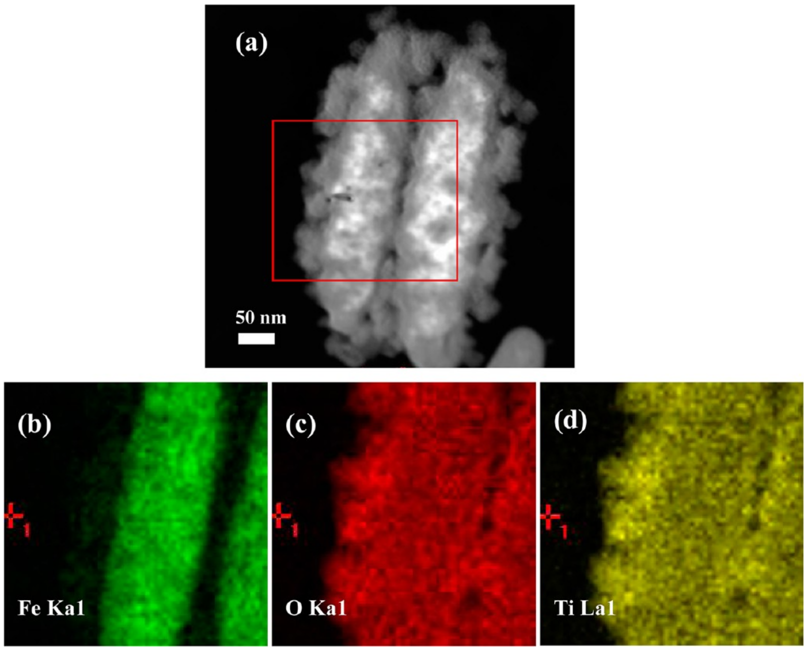

Figure 4. (a) HAADF-STEM image of α-Fe_2O_3@LTO-0.75 and element mapping of (b) Fe Ka1, (c) O Ka1, and (d) Ti La1.

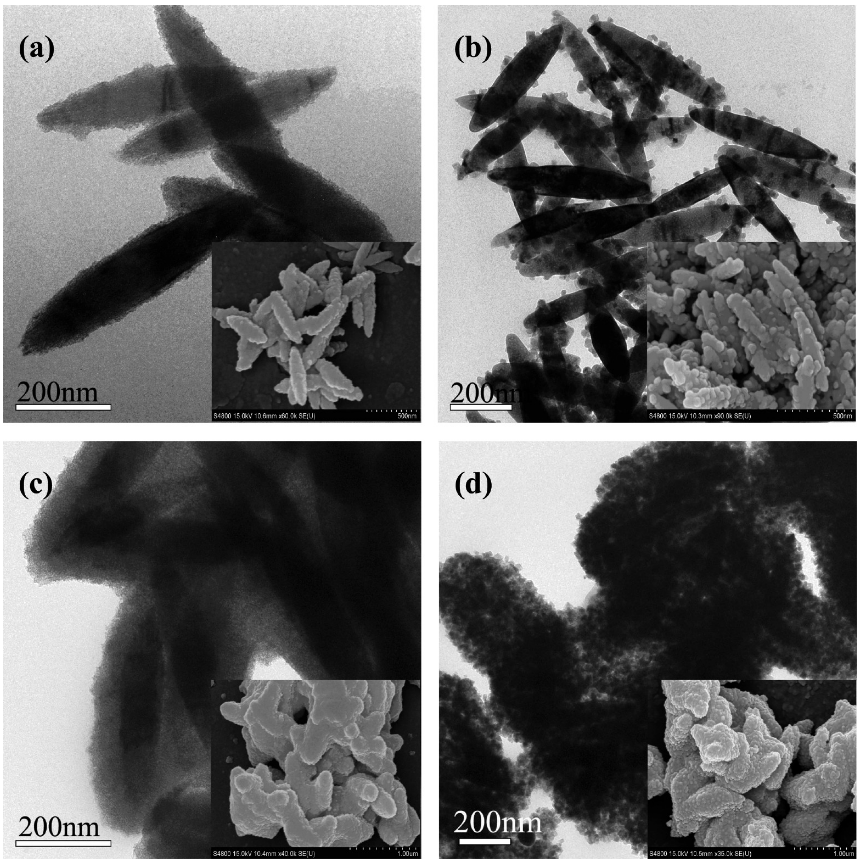

Figure 5. TEM and SEM images of (a) α-Fe_2O_3@TiO_2-0.5, (b) α-Fe_2O_3@LTO-0.5, (c) α-Fe_2O_3@TiO_2-1, and (d) α-Fe_2O_3@LTO-1.

intensity of diffraction peaks are in accordance with rhombohedral Fe_2O_3 and spinel lithium titanate, which confirms that the products are α-Fe_2O_3@LTO composites.

3.2.3. Effect of the Reaction Time. The time-dependent experiment was carried out to investigate the formation mechanism of the core−shell α-Fe_2O_3@LTO composite. The morphologies of the samples prepared with different reaction time are depicted in Figure 8. As shown in Figure 8b, at an earlier stage (0.5 h), the thin shells of TiO_2 turn into nanosheets due to the effect of hydroxyl. With the reaction process (Figure 8c, 1 h), many primary crystals appear and spontaneously aggregate the surface of α-Fe_2O_3. Simultane-

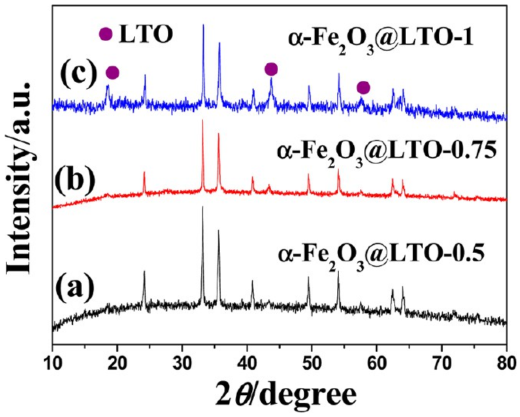

Figure 6. XRD patterns for α-Fe_2O_3@LTO obtained with different thickness TiO_2 shells: (a) α-Fe_2O_3@LTO-0.5, (b) α-Fe_2O_3@LTO-0.75, and (c) α-Fe_2O_3@LTO-1.

ously, the amount of nanosheets (red arrows) decreases. The sample collected 1.5 h later shows the α-Fe_2O_3 surface is coated with a great deal of nanocrystals (Figure 8d). After 2 h (Figure 8e), after Ostwald ripening, the large amount of small nanocrystals grow into big nanocrystals accompanying the disappearance of the nanosheets. When the reaction time is prolonged to 3 h, the sample reshapes the core−shell structure of α-Fe_2O_3@LTO composite.

On the basis of the above discussions, the possible formation mechanism of the core−shell α-Fe_2O_3@LTO composite in this paper could be clearly illustrated in Figure 9. At the initial period of the hydrothermal synthesis, TiO_2 reacts with LiOH under the basic condition and produces amorphous titanate, which shows nanosheets-shaped structure.[45,46] When NaOH replaced LiOH, the nanosheet-shaped structure coated on the surface of α-Fe_2O_3 was obtained (Figure S2, Supporting Information), which confirmed the reaction between hydrous titanium oxide and OH^-. The amorphous titanate nanosheets are easy to dehydrate at high temperature and generate small $Li_4Ti_5O_{12}$ nanocrystals. In order to decrease the surface free energy, these nanocrystals tend to aggregate on the surface of α-Fe_2O_3 easily to form the core−shell structure. Meanwhile, Ostwald ripening promotes the $Li_4Ti_5O_{12}$ crystals growth, and the sample eventually forms the core−shell structure of α-Fe_2O_3@LTO composite.

3.3. Electrochemical Performance of α-Fe_2O_3@LTO Composite. For the examination of the effects of LTO coating on the electrochemical performance of α-Fe_2O_3, α-Fe_2O_3 ellipsoids and α-Fe_2O_3@LTO composites with different shell thicknesses are used as the anodes in half cell measurements. Testing was carried out under constant current conditions (100 mA g^{-1}) in the 0.5−2.5 V voltage at room temperature. Figure 10A shows the first cycle discharge/charge curves of pure α-Fe_2O_3 ellipsoids and α-Fe_2O_3@LTO-0.75. The first cycle charge and discharge capacities of α-Fe_2O_3@LTO-0.75 are 609.2 and 791.3 mA h g^{-1}, respectively, whereas the corresponding values for the uncoated α-Fe_2O_3 ellipsoids are 565.2 and 875.8 mA h g^{-1} measured at the same current density. The overall initial capacity loss therefore decreases from 310.6 to 182.1 mA h g^{-1}. The first cycle discharge/charge

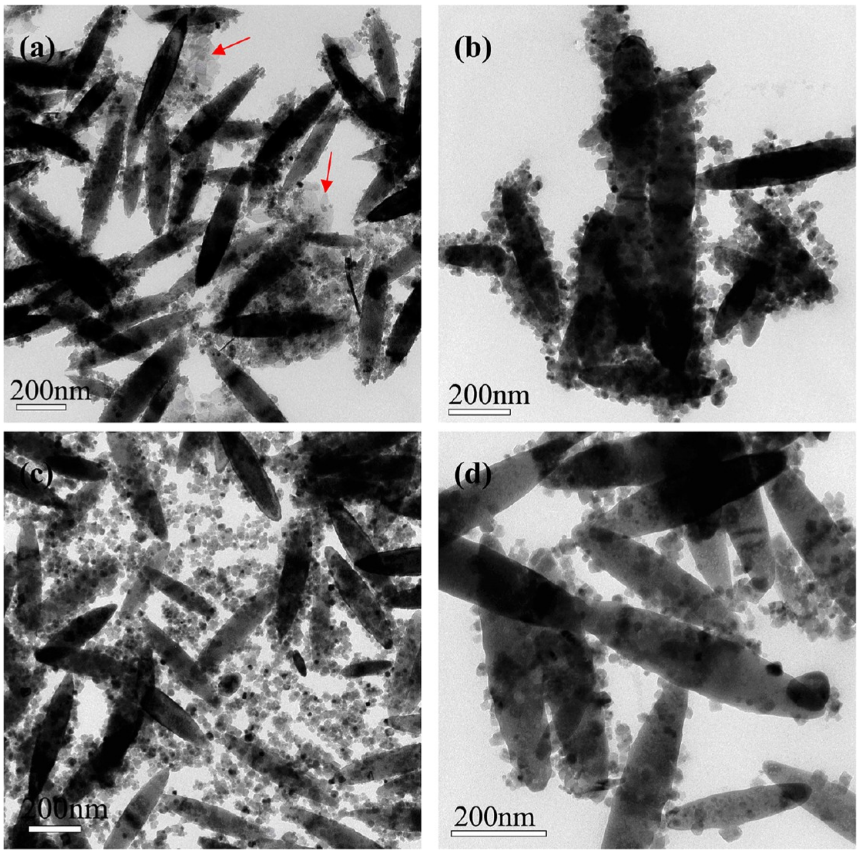

Figure 7. TEM images of α-Fe_2O_3@LTO-0.75 obtained at different temperature: (a),(b) 180°C; (c),(d) 210°C; (a),(c) before calcination; and (b),(d) after calcination.

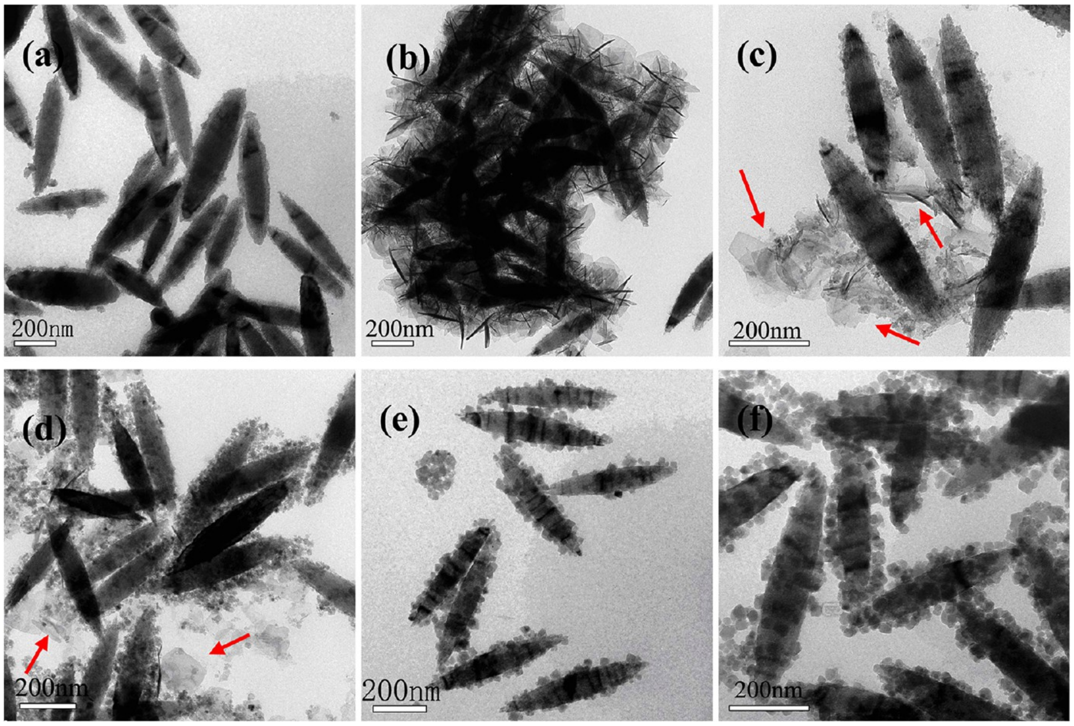

Figure 8. TEM images of the products collected at different reaction times: (a) 0 h, (b) 0.5 h, (c) 1 h, (d) 1.5 h, (e) 2 h, and (f) 3 h.

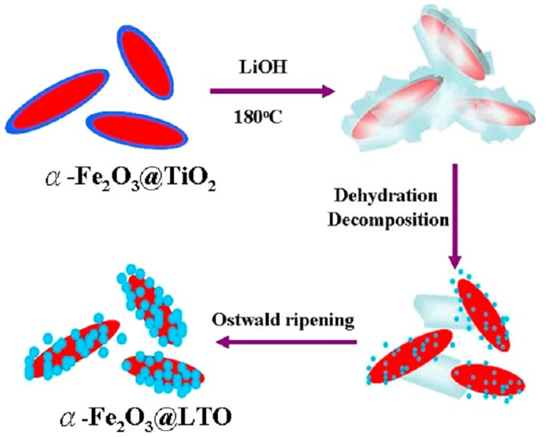

Figure 9. Schematic illustration for the plausible formation mechanism of the core−shell α-Fe_2O_3@LTO composite.

curves of α-Fe_2O_3@LTO-0.5 and α-Fe_2O_3@LTO-1.0 composites are similar in features. To some extent, the LTO shell might avoid reduction of electrolyte on the surface of the electrode, formation of a SEI layer, and a decrease in the initial capacity loss. With the increase of the LTO shell thickness, the tendency is obvious. For α-Fe_2O_3@LTO-0.5 composite with the smallest LTO content, α-Fe_2O_3 core are not heavily encapsulated by the LTO nanocrystals. The thin LTO shell in the current implementation cannot avoid the formation of a SEI layer and totally resists the volume excursion in the core area. The overall initial capacity loss of α-Fe_2O_3@LTO-0.5 (247.5 mA h g^{-1}) is larger than that of α-Fe_2O_3@LTO-0.75 (182.1 mA h g^{-1}). On the contrary, for α-Fe_2O_3@LTO-1 composite with dense LTO shell (80 nm thickness), the overall initial capacity loss is only 146.3 mA h g^{-1} and even smaller than that of α-Fe_2O_3@LTO-0.75. But, on the other hand, the intrinsic low capacity of LTO limits the capacity promotion of α-Fe_2O_3@LTO composite. For α-Fe_2O_3@LTO-1 composite with dense LTO shell (80 nm thickness), the first cycle discharge capacity is only 533.9 mA h g^{-1}, which is the smallest value in three composites because of its highest LTO content. Therefore, the suitable LTO shell thickness is the key factor for improving the electrochemical performance of α-Fe_2O_3@LTO composite. The Coulombic efficiencies of α-Fe_2O_3@LTO-0.75 (76.8%) are higher than α-Fe_2O_3 (62.9%) in the first cycle discharge/charge process. The representative cyclic voltammograms (CVs) of α-Fe_2O_3@LTO-0.75 between 5 mV and 3 V at a scan rate of 0.2 mV s^{-1} is shown in Figure S3B. In the cathodic polarization process of the first cycle, the peak is observed at 1.5V (vs. Li^+/Li), corresponding to the Li insertion into LTO and the formation of Li_2O. Meanwhile, in the anodic polarization process, only one peak is recorded at about 1.77 V (vs. Li^+/Li), which is attributed to the oxidation of Fe^0 to Fe^{3+}.[23] Obviously, the peak current decreases significantly in the second cycle, indicating the occurrence of some irreversible processes in the electrode material in the first cycle. When α-Fe_2O_3 ellipsoids used as electrode materials, the decrease of peak current in the second cycle becomes even more obvious (Figure S3A), which implies that α-Fe_2O_3@LTO-0.75 electrode materials exhibit better reversibility than α-Fe_2O_3 ellipsoids.

The cycling performance of the composites was also measured at 100 mA g^{-1}, and Figure 10B shows their comparison. The discharge capacity of uncoated α-Fe_2O_3 ellipsoids decreases to 74.2 mA h g^{-1} by the 30th cycle, whereas the corresponding value for α-Fe_2O_3@LTO-0.75 was 249.3 mA h g^{-1}. Subsequently, the discharge capacities for α-Fe_2O_3 ellipsoids and α-Fe_2O_3@LTO-0.75 decrease to 8.5% and 31.5%, respectively. The electrochemical performance of α-Fe_2O_3@TiO_2 composite has been studied by Zhao's group.[44] After 30 cycles at 0.5 C, the discharge capacity is about 200 mA h g^{-1}, which is smaller than α-Fe_2O_3@LTO. Although capacity decay could still be observed, the cycling performance of α-Fe_2O_3 ellipsoids with LTO coating layer reveal significant

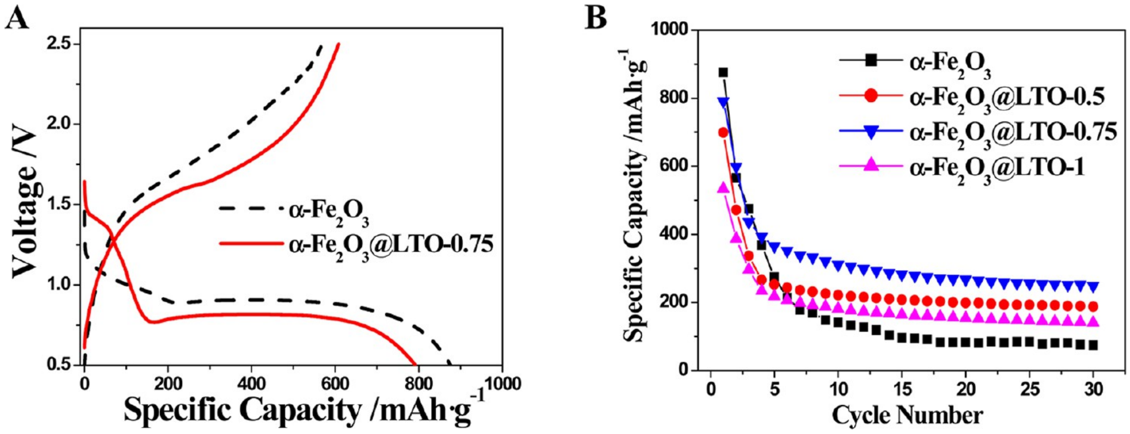

Figure 10. (A) Voltage profiles of α-Fe_2O_3 (calcined at 500°C) and α-Fe_2O_3@LTO-0.75 at 100 mA g^{-1} and (B) cycling performance of α-Fe_2O_3, α-Fe_2O_3@LTO-0.5, α-Fe_2O_3@LTO-0.75, and α-Fe_2O_3@LTO-1 at 100 mA g^{-1}.

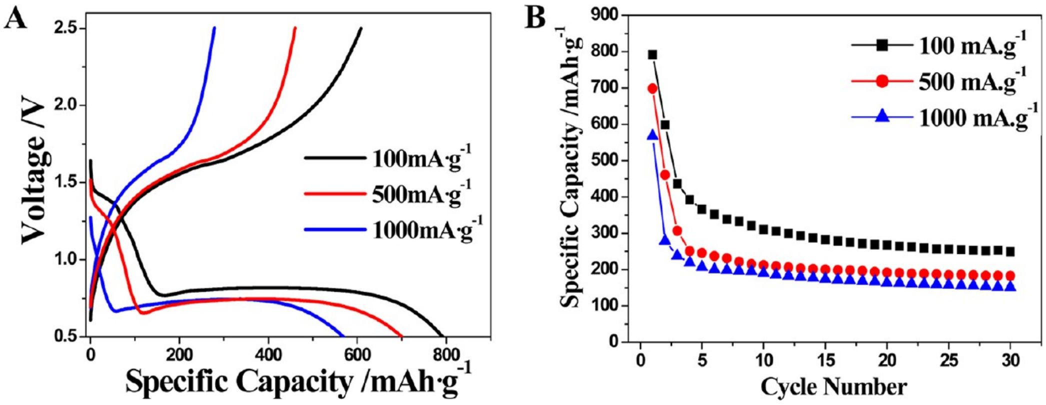

Figure 11. (A) Voltage profiles of α-Fe_2O_3@LTO-0.75 at different current density and (B) cycling performance of α-Fe_2O_3@LTO-0.75 at different current density.

improvements over the uncoated α-Fe_2O_3 ellipsoids, which is attributed to excellent reversibility of spinel $Li_4Ti_5O_{12}$ with zero strain property in lithium insertion/extraction reactions. However, the capacity decay is mostly caused by the formation of a SEI layer on the electrode material in some irreversible processes and the exfoliation of the LTO nanocrystals after repetitive expansion and contraction of the anode.[39,40] The morphology of α-Fe_2O_3@LTO-0.75 after 30 cycles was shown in Figure S4 (Supporting Information). The results show some LTO nanoparticles drop from the surface of α-Fe_2O_3 cores, but the core−shell structure of α-Fe_2O_3@LTO is still retained.

Figure 11A shows the first cycle charge−discharge curves of α-Fe_2O_3@LTO-0.75 under different current densities. The overall initial capacity loss at 500 and 1000 mA g^{-1} is 241.6 and 289.2 mA h g^{-1}, respectively. With the increase of current densities, the overall initial capacity loss increases. Then, the cycling performance of α-Fe_2O_3@LTO-0.75 under different current densities is shown in Figure 11B. After the 30th cycle, the discharge capacities of α-Fe_2O_3@LTO-0.75 are 182.3 and 151.5 mA h g^{-1} for 500 and 1000 mA g^{-1}, respectively. At 500 and 1000 mA g^{-1}, the values of the Coulombic efficiencies are 65.8% and 49.1% in the first cycle discharge/charge process, respectively. With the increase of current densities, the Coulombic efficiencies decline. As a comparison, α-Fe_2O_3@LTO-0.75 at lower current densities (100 mA g^{-1}) shows more excellent cycling performance. Despite, the LTO shell displays some evidence of resisting the formation of a SEI layer and decreasing the overall initial capacity loss, but its kinetic problems with low electrical conductivity (ca. 10^{-13} S cm^{-1}) and lithium diffusion coefficient (ca. 10^{-9} to 10^{-13} cm^2 s^{-1}) hinder the further improvement of the battery performance at higher current densities.[47−49]

The first cycle charge−discharge curves and the cycling performance of α-Fe_2O_3@LTO-0.75 obtained at different temperature are show in Figure S5 (Supporting Information). For two samples obtained at 150 and 210 °C, the overall initial capacity loss are 283.5 and 319.4 mA h g^{-1}, respectively. Higher initial capacity loss is ascribed to the poor coating of LTO shell. TEM images in Figure 7 confirm the inference. The Coulombic efficiencies of α-Fe_2O_3@LTO-0.75 obtained at 150 and 210 °C are 54.6% and 47.3% in the first cycle discharge/charge process, respectively. Compared with the samples as-prepared at 150 °C and 210 °C, the advantage of α-Fe_2O_3@LTO-0.75 as-prepared at 180 °C for Li ion storage is very apparent. Therefore, through the battery performance test, the electrochemical performance of α-Fe_2O_3@LTO composite heavily depends on the thickness and density of LTO-coating shells. Through further research, the novel LTO coating can be optimized to improve the electrochemical performance of other high capacity anode materials.

4. CONCLUSIONS

In conclusion, α-Fe_2O_3@$Li_4Ti_5O_{12}$ core−shell composites with different shell thicknesses were prepared. These α-Fe_2O_3@

$Li_4Ti_5O_{12}$ composites exhibit high specific capacities and cycling performances, especially the α-Fe_2O_3@LTO-0.75, when used as anode materials in Li ion batteries. The LTO coating shielded most of the direct contact between α-Fe_2O_3 and the electrolyte, and hence the initial capacity loss due to SEI formation was reduced to mostly that of LTO, which is much lower than naked α-Fe_2O_3. The cycling performance of α-Fe_2O_3@LTO composites was also a significant improvement. The discharge capacity of naked α-Fe_2O_3 was only 74.2 mA h g^{-1} in the 30th cycle, whereas the corresponding value for α-Fe_2O_3@LTO-0.75 was 249.3 mA h g^{-1}. The carbon-free coating of LTO is not only proved to be highly effective and more secure, but also promises high surface stability and long cycle life electrode materials. Therefore, the strategy may also be extended to other high capacity anode and cathode materials for future high energy/power density Li ion batteries used in electric vehicles and large-scale energy storage.

■ ASSOCIATED CONTENT

Ⓢ Supporting Information

XRD patterns for α-Fe_2O_3@LTO-0.75 prepared at different reaction temperature, TEM image of the reaction product between α-Fe_2O_3@TiO_2-0.75 and NaOH, cyclic voltammograms (CVs) of α-Fe_2O_3@LTO-0.75, the morphology of α-Fe_2O_3@LTO-0.75 after 30 cycles, voltage profiles and cycling performance of α-Fe_2O_3@LTO-0.75 prepared at different reaction temperature. This material is available free of charge via the Internet at http://pubs.acs.org.

■ AUTHOR INFORMATION

Corresponding Author

*E-mail: gwdiao@yzu.edu.cn. Fax: +86 514 87975244. Tel.: +86 514 87975436.

Notes

The authors declare no competing financial interest.

■ ACKNOWLEDGMENTS

The authors acknowledge the financial support from the National Natural Science Foundation of China (grant no. 20901065 and 21273195), the Project Funded by the Priority Academic Program Development of Jiangsu Higher Education Institutions, and the Natural Science Foundation of Education Committee of Jiangsu Province (12KJB150023).

■ REFERENCES

(1) Tarascon, J.-M.; Armand, M. Issues and Challenges Facing Rechargeable Lithium Batteries. *Nature* **2001**, *414*, 359−367.

(2) Lee, Y. J.; Yi, H.; Kim, W.-J.; Kang, K.; Yun, D. S.; Strano, M. S.; Ceder, G.; Belcher, A. M. Fabricating Genetically Engineered High-Power Lithium-Ion Batteries Using Multiple Virus Genes. *Science* **2009**, *324*, 1051−1055.

(3) Cheng, F.; Liang, J.; Tao, Z.; Chen, J. Functional Materials for Rechargeable Batteries. *Adv. Mater.* **2011**, *23*, 1695−1715.

(4) Wu, Z.; Yu, K.; Zhang, S.; Xie, Y. Hematite Hollow Spheres with a Mesoporous Shell: Controlled Synthesis and Applications in Gas Sensor and Lithium Ion Batteries. *J. Phys. Chem. C* **2008**, *112*, 11307−11313.

(5) Park, M.-S.; Kang, Y.-M.; Wang, G.-X.; Dou, S.-X.; Liu, H.-K. The Effect of Morphological Modification on the Electrochemical Properties of SnO_2 Nanomaterials. *Adv. Funct. Mater.* **2008**, *18*, 455−461.

(6) Yu, Y.; Chen, C.-H.; Shi, Y. A Tin-Based Amorphous Oxide Composite with a Porous, Spherical, Multideck-Cage Morphology as a Highly Reversible Anode Material for Lithium-Ion Batteries. *Adv. Mater.* **2007**, *19*, 993−997.

(7) Idota, Y.; Kubota, T.; Matsufuji, A.; Maekawa, Y.; Miyasaka, T. Tin-Based Amorphous Oxide: A High-Capacity Lithium-Ion-Storage Material. *Science* **1997**, *276*, 1395−1397.

(8) Taberna, P. L.; Mitra, S.; Poizot, P.; Simon, P.; Tarascon, J.-M. High Rate Capabilities Fe_3O_4-Based Cu Nano-Architectured Electrodes for Lithium-Ion Battery Applications. *Nat. Mater.* **2006**, *5*, 567−573.

(9) Yuan, S. M.; Li, J. X.; Yang, L. T.; Su, L. W.; Liu, L.; Zhou, Z. Preparation and Lithium Storage Performances of Mesoporous Fe_3O_4@C Microcapsules. *ACS Appl. Mater. Interfaces* **2011**, *3*, 705−709.

(10) Chen, J. S.; Zhang, Y.; Lou, X. W. One-Pot Synthesis of Uniform Fe_3O_4 Nanospheres with Carbon Matrix Support for Improved Lithium Storage Capabilities. *ACS Appl. Mater. Interfaces* **2011**, *3*, 3276−3279.

(11) Chen, D.; Ji, G.; Ma, Y.; Lee, J. Y.; Lu, J. Graphene-Encapsulated Hollow Fe_3O_4 Nanoparticle Aggregates As a High-Performance Anode Material for Lithium Ion Batteries. *ACS Appl. Mater. Interfaces* **2011**, *3*, 3078−3083.

(12) Yuan, C.; Wu, H. B.; Xie, Y.; Lou, X. W. Mixed Transition-Metal Oxides: Design, Synthesis, and Energy-Related Applications. *Angew. Chem., Int. Ed.* **2014**, *53*, 1488−1504.

(13) Wu, H. B.; Chen, J. S.; Hng, H. H.; Lou, X. W. Nanostructured Metal Oxide-Based Materials as Advanced Anodes for Lithium-Ion Batteries. *Nanoscale* **2012**, *4*, 2526−2542.

(14) Wang, B.; Wu, H. B.; Zhang, L.; Lou, X. W. Self-Supported Construction of Uniform Fe_3O_4 Hollow Microspheres from Nanoplate Building Blocks. *Angew. Chem., Int. Ed.* **2013**, *52*, 4165−4168.

(15) Reddy, M. V.; Yu, T.; Sow, C. H.; Shen, Z. X.; Lim, C. T.; Subba Rao, G. V.; Chowdari, B. V. R. α-Fe_2O_3 Nanoflakes as an Anode Material for Li-Ion Batteries. *Adv. Funct. Mater.* **2007**, *17*, 2792−2799.

(16) Wang, P. C.; Ding, H. P.; Bark, T.; Chen, C. H. Nanosized α-Fe_2O_3 and Li−Fe Composite Oxide Electrodes for Lithium-Ion Batteries. *Electrochim. Acta* **2007**, *52*, 6650−6655.

(17) Wang, Z.; Zhou, L.; Lou, X. W. Metal Oxide Hollow Nanostructures for Lithium-Ion Batteries. *Adv. Mater.* **2012**, *24*, 1903−1911.

(18) Koo, B.; Xiong, H.; Slater, M. D.; Prakapenka, V. B.; Balasubramanian, M.; Podsiadlo, P.; Johnson, C. S.; Rajh, T.; Shevchenko, E. V. Hollow Iron Oxide Nanoparticles for Application in Lithium Ion Batteries. *Nano Lett.* **2012**, *12*, 2429−2435.

(19) Cherian, C. T.; Sundaramurthy, J.; Kalaivani, M.; Ragupathy, P.; Kumar, P. S.; Thavasi, V.; Reddy, M. V.; Sow, C. H.; Mhaisalkar, S. G.; Ramakrishna, S.; et al. Electrospun α-Fe_2O_3 Nanorods as a Stable, High Capacity Anode Material for Li-Ion Batteries. *J. Mater. Chem.* **2012**, *22*, 12198−12204.

(20) Chen, J.; Xu, L.; Li, W.; Gou, X. α-Fe_2O_3 Nanotubes in Gas Sensor and Lithium-Ion Battery Applications. *Adv. Mater.* **2005**, *17*, 582−586.

(21) Wu, C.; Yin, P.; Zhu, X.; OuYang, C.; Xie, Y. Synthesis of Hematite (α-Fe_2O_3) Nanorods: Diameter-Size and Shape Effects on Their Applications in Magnetism, Lithium Ion Battery, and Gas Sensors. *J. Phys. Chem. B* **2006**, *110*, 17806−17812.

(22) Zeng, S.; Tang, K.; Li, T.; Liang, Z.; Wang, D.; Wang, Y.; Qi, Y.; Zhou, W. Facile Route for the Fabrication of Porous Hematite Nanoflowers: Its Synthesis, Growth Mechanism, Application in the Lithium Ion Battery, and Magnetic and Photocatalytic Properties. *J. Phys. Chem. C* **2008**, *112*, 4836−4843.

(23) Wang, B.; Chen, J. S.; Wu, H. B.; Wang, Z.; Lou, X. W. Quasiemulsion-Templated Formation of α-Fe_2O_3 Hollow Spheres with Enhanced Lithium Storage Properties. *J. Am. Chem. Soc.* **2011**, *133*, 17146−17148.

(24) Zhang, L.; Wu, H. B.; Lou, X. W. Iron-Oxide-Based Advanced Anode Materials for Lithium-Ion Batteries. *Adv. Energy Mater.* **2014**, DOI: 10.1002/aenm.201300958.

(25) Goodenough, J. B.; Kim, Y. Challenges for Rechargeable Li Batteries. *Chem. Mater.* **2010**, *22*, 587−603.

(26) Peled, E. Improved Graphite Anode for Lithium-Ion Batteries Chemically. *J. Electrochem. Soc.* **1996**, *143*, L4.

(27) Zhang, S. S. A Review on Electrolyte Additives for Lithium-Ion Batteries. *J. Power Sources* **2006**, *162*, 1379−1394.

(28) Zhu, X.; Zhu, Y.; Murali, S.; Stoller, M. D.; Ruoff, R. S. Nanostructured Reduced Graphene Oxide/Fe_2O_3 Composite As a High-Performance Anode Material for Lithium Ion Batteries. *ACS Nano* **2011**, *5*, 3333−3338.

(29) Wang, D.; Kou, R.; Choi, D.; Yang, Z.; Nie, Z.; Li, J.; Saraf, L. V.; Hu, D.; Zhang, J.; Graff, G. L.; et al. Ternary Self-Assembly of Ordered Metal Oxide−Graphene Nanocomposites for Electrochemical Energy Storage. *ACS Nano* **2010**, *4*, 1587−1595.

(30) Ji, L.; Lin, Z.; Alcoutlabi, M.; Zhang, X. Recent Developments in Nanostructured Anode Materials for Rechargeable Lithium-Ion Batteries. *Energy Environ. Sci.* **2011**, *4*, 2682−2699.

(31) Zhou, W.; Cheng, C.; Liu, J.; Tay, Y. Y.; Jiang, J.; Jia, X.; Zhang, J.; Gong, H.; Hng, H. H.; Yu, T.; et al. Epitaxial Growth of Branched α-Fe_2O_3/SnO_2 Nano-Heterostructures with Improved Lithium-Ion Battery Performance. *Adv. Funct. Mater.* **2011**, *21*, 2439−2445.

(32) Ma, Y.; Ding, B.; Ji, G.; Lee, J. Y. Carbon-Encapsulated F-Doped $Li_4Ti_5O_{12}$ as a High Rate Anode Material for Li^+ Batteries. *ACS Nano* **2013**, *7*, 10870−10878.

(33) Shen, L.; Yuan, C.; Luo, H.; Zhang, X.; Chen, L.; Li, H. Novel Template-Free Solvothermal Synthesis of Mesoporous $Li_4Ti_5O_{12}$-C Microspheres for High Power Lithium Ion Batteries. *J. Mater. Chem.* **2011**, *21*, 14414−14416.

(34) Shen, L.; Yuan, C.; Luo, H.; Zhang, X.; Xu, K.; Xia, Y. Facile Synthesis of Hierarchically Porous $Li_4Ti_5O_{12}$ Microspheres for High Rate Lithium Ion Batteries. *J. Mater. Chem.* **2010**, *20*, 6998−7004.

(35) Jung, H.-G.; Jang, M. W.; Hassoun, J.; Sun, Y.-K.; Scrosati, B. A High-Rate Long-Life $Li_4Ti_5O_{12}$/$Li[N_{i0.45}Co_{0.1}Mn_{1.45}]O_4$ Lithium-Ion Battery. *Nat. Commun.* **2011**, *2*, 516.

(36) Shen, L.; Yuan, C.; Luo, H.; Zhang, X.; Xu, K.; Zhang, F. In Situ Growth of $Li_4Ti_5O_{12}$ on Multi-Walled Carbon Nanotubes: Novel Coaxial Nanocables for High Rate Lithium Ion Batteries. *J. Mater. Chem.* **2010**, *21*, 761−767.

(37) Armand, M.; Tarascon, J.-M. Building Better Batteries. *Nature* **2008**, *451*, 652−657.

(38) Belharouak, I.; Sun, Y.-K.; Lu, W.; Amine, K. On the Safety of the $Li_4Ti_5O_{12}$/ $LiMn_2O_4$ Lithium-Ion Battery System. *J. Electrochem. Soc.* **2007**, *154*, A1083−A1087.

(39) Ohzuku, T. Zero-Strain Insertion Material of $Li[Li_{1/3}Ti_{5/3}]O_4$ for Rechargeable Lithium Cells. *J. Electrochem. Soc.* **1995**, *142*, 1431.

(40) Ariyoshi, K.; Yamato, R.; Ohzuku, T. Zero-Strain Insertion Mechanism of $Li[Li_{1/3}Ti_{5/3}]O_4$ for Advanced Lithium-Ion (shuttlecock) Batteries. *Electrochim. Acta* **2005**, *51*, 1125−1129.

(41) Ji, G.; Ma, Y.; Ding, B.; Lee, J. Y. Improving the Performance of High Capacity Li-Ion Anode Materials by Lithium Titanate Surface Coating. *Chem. Mater.* **2012**, *24*, 3329−3334.

(42) Wang, Y.-Q.; Gu, L.; Guo, Y.-G.; Li, H.; He, X.-Q.; Tsukimoto, S.; Ikuhara, Y.; Wan, L.-J. Rutile-TiO_2 Nanocoating for a High-Rate $Li_4Ti_5O_{12}$ Anode of a Lithium-Ion Battery. *J. Am. Chem. Soc.* **2012**, *134*, 7874−7879.

(43) Yu, L.; Wu, H. B.; Lou, X. W. Mesoporous $Li_4Ti_5O_{12}$ Hollow Spheres with Enhanced Lithium Storage Capability. *Adv. Mater.* **2013**, *25*, 2296−2300.

(44) Li, W.; Yang, J.; Wu, Z.; Wang, J.; Li, B.; Feng, S.; Deng, Y.; Zhang, F.; Zhao, D. A Versatile Kinetics-Controlled Coating Method To Construct Uniform Porous TiO_2 Shells for Multifunctional Core−Shell Structures. *J. Am. Chem. Soc.* **2012**, *134*, 11864−11867.

(45) Tang, Y.; Yang, L.; Qiu, Z.; Huang, J. Template-Free Synthesis of Mesoporous Spinel Lithium Titanate Microspheres and Their Application in High-Rate Lithium Ion Batteries. *J. Mater. Chem.* **2009**, *19*, 5980−5984.

(46) Tang, Y.; Yang, L.; Fang, S.; Qiu, Z. $Li_4Ti_5O_{12}$ Hollow Microspheres Assembled by Nanosheets as an Anode Material for High-Rate Lithium Ion Batteries. *Electrochim. Acta* **2009**, *54*, 6244−6249.

(47) Cheng, L.; Li, X.-L.; Liu, H.-J.; Xiong, H.-M.; Zhang, P.-W.; Xia, Y.-Y. Carbon-Coated $Li_4Ti_5O_{12}$ as a High Rate Electrode Material for Li-Ion Intercalation. *J. Electrochem. Soc.* **2007**, *154*, A692−A697.

(48) Cheng, L.; Yan, J.; Zhu, G.-N.; Luo, J.-Y.; Wang, C.-X.; Xia, Y.-Y. General Synthesis of Carbon-Coated Nanostructure $Li_4Ti_5O_{12}$ as a High Rate Electrode Material for Li-Ion Intercalation. *J. Mater. Chem.* **2009**, *20*, 595−602.

(49) Li, C. C.; Li, Q. H.; Chen, L. B.; Wang, T. H. A Facile Titanium Glycolate Precursor Route to Mesoporous Au/$Li_4Ti_5O_{12}$ Spheres for High-Rate Lithium-Ion Batteries. *ACS Appl. Mater. Interfaces* **2012**, *4*, 1233−1238.